scientific reports

Check for updates

OPEN

A microfluidics platform for simultaneous evaluation of sensitivity and side effects of anti-cancer drugs using a three-dimensional culture method

Yuki Kobayashi[1], Honoka Hashizume[1], Sotaro Takiguchi[2], Jiajue Ji[2], Ryuji Kawano[2], Keiichiro Koiwai[3], Haru Yamamoto[1,4], Mohamed Elbadawy[1,5,6]✉, Tsutomu Omatsu[7], Amira Abugomaa[1,8], Masahiro Kaneda[9], Tatsuya Usui[1]✉ & Kazuaki Sasaki[1]

Organoids are stem cell-derived three-dimensional tissue cultures composed of multiple cell types that recapitulate the morphology and functions of their in vivo counterparts. Organ-on-a-chip devices are tiny chips with interconnected wells and channels designed using a perfusion system and microfluidics to precisely mimic the in vivo physiology and mechanical forces experienced by cells in the body. These techniques have recently been used to reproduce the structure and function of organs in vitro and are expected to be promising alternatives for animal experiments in the future. In the present study, we designed and fabricated an organ-on-a-chip system for mounting organoids from mammary tumor-affected cats (FMT organoids) and normal intestinal organoids from mice (MI organoids) and perfused them with anti-cancer drugs. The effects of drug perfusion on FMT and MI organoids were examined by measuring cell viability and performing genetic analysis. After 48 h of perfusion with toceranib (10 µM) or doxorubicin (1 µM), cell viability of FMT organoids was decreased compared to the non-perfusion condition. The expression of apoptosis-related genes, such as *p53* and *Caspase-9* was significantly upregulated in FMT organoids with drug perfusion. The rate of cell death drastically differed before and after branching in the device, owing to differences in flow velocity and drug infiltration. Perfusion of MI organoids with toceranib also reduced viability, as observed in FMT organoids; however, this was due to the induction of necrosis rather than apoptosis. In conclusion, our established multi-organoid-on-chip system could be used to evaluate anti-cancer drug sensitivity and side effects in vitro, which might contribute to developing personalized medicine for cancer patients.

Keywords Organoid, Organ-on-chip, Feline mammary tumor, Anti-cancer drug, Microfluidic device, Side effects

Malignant tumors are the most common cause of death in dogs and cats. They account for one-third of all cat deaths, with mammary tumors being the most common in cats aged 10–12 years[1,2]. Surprisingly, about 80%

[1]Laboratory of Veterinary Pharmacology, Department of Veterinary Medicine, Faculty of Agriculture, Tokyo University of Agriculture and Technology, 3-5-8 Saiwai-cho, Fuchu , Tokyo 183-8509, Japan. [2]Department of Biotechnology and Life Science, Faculty of Technology, Tokyo University of Agriculture and Technology, 2-24-16 Naka-machi, Higashi Koganei, Tokyo 184-8588, Japan. [3]Laboratory of Genome Science, Department of Undergraduate Course of Marine Biosciences, Tokyo University of Marine Science and Technology, 4-5-7 Konan, Minato-ku, Tokyo 108-8477, Japan. [4]AIRDEC Mini Co., Ltd., 1-2-36 Kajino-cho, Koganei, Tokyo 184-0002, Japan. [5]Department of Pharmacology, Faculty of Veterinary Medicine, Benha University, Moshtohor, Toukh 13736, Elqaliobiya, Egypt. [6]Precision One Health Initiative, Department of Pathology, College of Veterinary Medicine, University of Georgia, Athens, GA 30602, USA. [7]Center for Infectious Disease Epidemiology and Prevention Research, Tokyo University of Agriculture and Technology, 3-5-8 Saiwai-Cho, Fuchu, Tokyo 183-8509, Japan. [8]Faculty of Veterinary Medicine, Mansoura University, Mansoura 35516, Egypt. [9]Laboratory of Veterinary Anatomy, Department of Veterinary Medicine, Faculty of Agriculture, Tokyo University of Agriculture and Technology, 3-5-8 Saiwai-cho, Fuchu, Tokyo 183-8509, Japan. ✉email: Mohamed.elbadawy@fvtm.bu.edu.eg; fu7085@go.tuat.ac.jp

of mammary tumors in cats are malignant with a high tendency to metastasize, and the percentage of cats with lymph node metastasis already present at the time of initial diagnosis is very high, ranging from 20 to 42%[1,3,4]. Although tumors are graded according to size and presence of metastasis, the prognosis is poor, with a median survival of approximately 30 months for low-grade tumors and 8 months for high-grade tumors[5]. Additionally, spontaneous feline mammary tumors (FMT) are considered a natural model of human aggressive breast carcinoma (HBCs) as they both share wide demographic, epidemiological, and clinicopathologic similarities[6–9]. Under the criterion of the WHO classification of mammary tumors, HBCs are simple glandular epithelial tumors. In this context, FMT demonstrates a high similarity to HBCs since in cats the vast majority of FMT are malignant glandular epithelial tumors[10]. Cats with mammary tumors are usually treated by removal of the mammary glands. As mammary glands are interconnected by lymphatic vessels, the recurrence rate is high[11]. If a patient is diagnosed as a high-risk group for recurrence, chemotherapy with anti-cancer drugs such as doxorubicin and carboplatin is usually performed after surgery[12]. The use of anti-cancer drugs in cats with mammary tumors is associated with serious side effects. These include gastrointestinal toxicity, such as vomiting and anorexia; bone marrow toxicity, such as leukopenia and thrombocytopenia; and cardiotoxicity and nephrotoxicity, depending on the type of anti-cancer drug[5]. The sensitivity or resistance of cancer cells to anti-cancer drugs is of primary concern in anti-cancer therapy, and simultaneous evaluation of drug sensitivity and side effects in vitro is challenging.

Organoids (miniaturized organs) are stem cell-derived 3D cellular structures that can self-aggregate, renew, differentiate, and recapitulate the in vivo morphology and functions of the original tissues or organs[13–16]. Organoids showed great promise in organogenesis, drug screening, and disease modeling[14,17–23]. In previous studies, we established methods for culturing organoids from normal and cancerous tissues[24–28]. Organ-on-chip, also called organ-chip, tissue-chip, or microphysiology system, is a cell culture system designed to mimic the functions of multicellular tissues and organs[29,30]. By modeling the complex functions of living organisms, these systems can reproduce cell–cell interactions and advanced physiological functions[31–33]. Recently, various organs and diseases have been modeled using various organ-on-chip devices[34,35–40]. Combining patient-derived cancer organoid cultures with the organ-on-a-chip system is expected to lead to the development of more practical clinical models[41,42].

In the present study, we generated FMT organoids and normal intestinal organoids from mice (MI organoids) and loaded them onto a microfluidic device to investigate the effects of anti-cancer drug perfusion on the viability of FMT organoids and to evaluate their side effects on MI organoids.

Materials and methods

Materials

To generate FMT and MI organoids, cells extracted from tissue samples were mixed with Matrigel (BD Bioscience, San Jose, CA, USA) and cultured in a stem cell-supporting medium as described previously[24,25,28]. FMT samples were portions of mammary tumor tissues from a patient cat that were surgically removed at veterinary clinics (Minamigaoka Animal Hospital) in Japan, transported immediately to the laboratory in a shipping medium[26,27] and used to generate FMT organoids. The experiments were approved by the Institutional Animal Care and Use Committee of Tokyo University of Agriculture and Technology (approval number: 0020007). Mouse experiments were also performed following the guidelines of the Institutional Animal Care and Use Committee of the Tokyo University of Agriculture and Technology (approval number: R04-120). Female C57BL/6 J mice (6 week-old) were obtained from Japan SLC Inc. (Shizuoka, Japan). The mice were anesthetized by isoflurane and the intestinal tissues were dissected and used for generating MI organoids. The studies were also done in agreement with Animal Research: Reporting of In Vivo Experiments (ARRIVE) guidelines.

The anti-cancer drugs used included doxorubicin (Cayman, Ann Arbor, MI, USA) and toceranib sulfate (Sigma-Aldrich, Saint Louis, MO, USA). The antibody source used was HER2 (Novus Biologicals Inc., Centennial CO., USA), whereas the necrosis inhibitor was HS-1371 (MedChem Express Inc., Monmouth, NJ, USA). The fluorescent secondary antibodies used were as follows: Alexa Fluor™ 488 donkey anti-goat IgG; Alexa Fluor 488™ goat anti-rabbit IgG; Alexa Fluor 488™ goat anti-mouse IgG (all Thermo Fisher Scientific Inc., Waltham, MA, USA); Biotinylated goat anti-mouse IgG (Vector Laboratories Inc., Newark, CA, USA); Horseradish peroxidase (HRP)-conjugated anti-rabbit IgG (Cayman); and HRP-conjugated anti-mouse IgG (Millipore, Temecula, CA, USA).

The secondary antibody used for IHC was Dako Envision + dual Link System-HRP (Catalog #: K4061, Agilent Technologies Inc., Santa Clara, CA, USA), and visualized using DAB solution (Nacalai Tesque, Tokyo, Japan).

Fabrication of the microfluidic device

The microfluidic device was fabricated using mechanical micromachining. First, a 3D device design was created using computer-aided design (CAD) software and converted into CNC milling paths using computer-aided manufacturing (CAM) software. The detailed dimensions of the device are provided in Fig. 1C and Supplemental Fig. 1 (unit: mm). A 2 mm thick acrylic sheet was machined to create microfluidic channels using a CNC milling machine (MiniMiller MM100, Modia Systems Co., Ltd., Japan). Two different drill bits, with diameters of 0.4 and 0.5 mm (MHR230, NS Tool Co., Ltd., Japan), were used to mill various parts of the microfluidic structure, including inlets, outlets, chambers, and channels, to achieve the required dimensions. After milling the microfluidic features, a 1 mm diameter drill bit (MHR230, NS Tool Co., Ltd., Japan) was used to segment the acrylic sheet into individual sections, each measuring 3 × 4 cm and containing a complete microfluidic channel network. The bases for the microfluidic device were prepared by machining another 2 mm-thick acrylic sheet into 3 × 4 cm blocks.

Thermal bonding was used to assemble the microfluidic device. A hot press (ROMANOFF, USA) was used to apply heat and pressure, which softened the acrylic at the interface and created robust bonds. Before bonding,

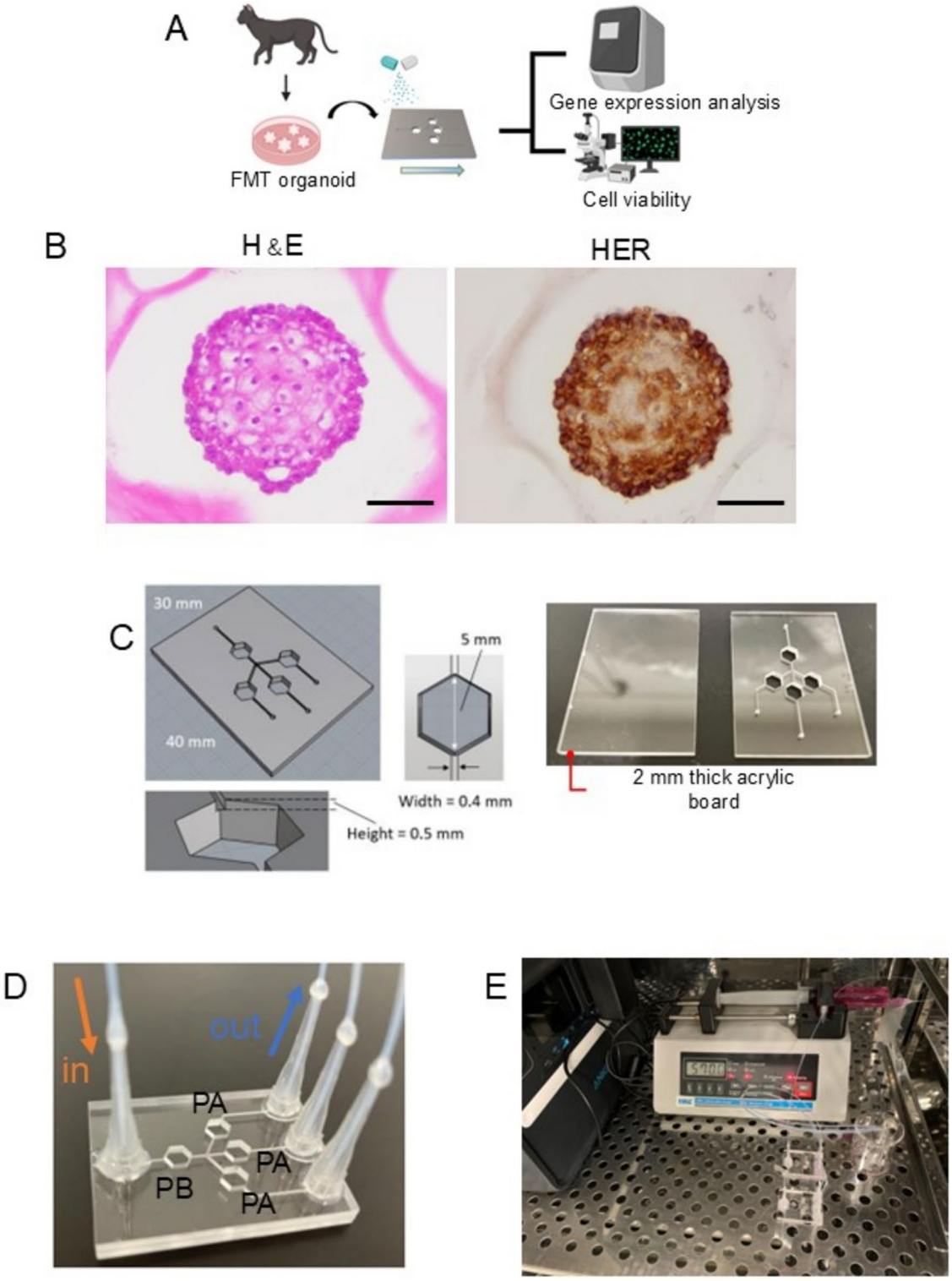

Fig. 1. Establishment of a microfluidic system using an organ-on-chip system and feline mammary tumor (FMT) organoids. Overview of organoids-on-a-chip experiments (**A**). Representative H&E-stained image (Left panel) and expression of a mammary tumor marker HER2 (Right panel) in FMT organoids are shown (**B**). Scale bar: 50 μm. After generating organoids from a cat with mammary tumor disease, the organoids were mounted on a microfluidic device, and drug perfusion was performed. After perfusion, the organoids were collected for genetic analysis and cell survival measurements. The device was created by CAD design and acrylic cutting. The width and height of the flow channel were 0.4 and 0.5 mm, respectively, and the diameter of the chamber was set at 5 mm (**C**). Liquid flows in from the left side of the device and flows out in three separate directions (**D**). The device was connected to a syringe pump and perfused in a CO_2 incubator at 37 ℃ for 48 h (**E**).

residual debris within the microchannels was carefully removed using tweezers or adhesive tape to ensure channel clarity. The channel sections were then aligned with the base blocks and secured in position using high-temperature-resistant tape to prevent movement during the bonding process. Glass plates were placed on either side of the assembly to prevent the acrylic material from adhering to the metal plates of the hot press during bonding. The bonding was conducted at 215 °C for 21 min.

The connectors for the inlet and outlet of the microfluidic device were fabricated by cutting the tips off the pipettes and inserting 0.75 mm diameter PTFE tubes (F-8007-001, Fron Industry, Japan) into the tips. The tips were secured with a strong adhesive (High Super 5, Cemedine, Japan). The connectors were then affixed to the inlet and outlet of the microfluidic device. After assembly, the device was left undisturbed overnight to allow the adhesive to fully cure.

Generation and culture of FMT and MI organoids

To prepare the FMT and MI organoids, mammary tumor and intestinal tissues collected from cats with mammary tumors and normal mice, respectively, were cut and washed three times with PBS (Takara Bio Inc., Shiga, Japan). Mice were euthanized under isoflurane anesthesia and the tissues were isolated. After washing, the tissues were minced finely, mixed in 0.1 mg/mL LiberaseTH (Sigma-Aldrich), and shaken in a 37 ℃ thermostatic bath for 30 min. They were then centrifuged at 600 × *g* for 3 min, removing the supernatant. After they were trypsinized in a thermostatic bath at 37 ℃ for 5 min, they were passed through a 70 µm pore size nylon cell strainer, collected in a 15 mL tube with fetal bovine serum (FBS, Sigma-Aldrich), and centrifuged for 3 min. After centrifugation, the supernatant was removed and the cells were washed three times with PBS. The supernatant was then aspirated and the cell pellet was suspended in Matrigel on ice and dropped into wells of a 24-well plate at 40 µL droplet size. After the gel was allowed to solidify in a CO_2 incubator at 37 °C for 30 min, the organoid culture medium was added (500 µL per well) and the culture plates were maintained at 37 ℃ under 5% CO_2. The medium was changed three times per week.

Organoid passage

After culturing the organoids for 7–14 days, they were passaged into new wells using 5 mM EDTA/PBS solution at a ratio of 1:3–4, depending on the size and density of the organoids in the wells. Briefly, to dissolve Matrigel, 500 µL of 5 mM EDTA/PBS was added per well and the culture plate was kept on ice for 90 min. The organoid suspension was collected in a 15 mL tube and centrifuged at 4 ℃ and 600 × *g* for 3 min. After washing the organoids with PBS, it was treated with 1 mL of pre-warmed (37 ℃) TrypLE Express solution (Life Technologies Co., Grand Island, NY, USA) for 5 min at 37 ℃ and vigorously pipetted, and 100 µL of FBS was added to the tube to neutralize the solution. Cell pellets were collected by centrifugation and mixed with fresh Matrigel on ice as described above. The Matrigel-containing cells were dropped on a 24-well plate at 40 µL/well, solidified in a CO_2 incubator at 37 ℃ for 30 min, and then the culture medium was added to each well and replaced three times weekly.

Hematoxylin and eosin (H&E) staining of FMT organoids

H&E staining of organoids was carried out as described previously[24,25]. After fixation overnight with 4% paraformaldehyde (4% PFA, FUJIFILM Wako Pure Chemical Corporation, Osaka, Japan), each organoid sample was dehydrated with ethanol and xylene and then embedded in paraffin for microtome slicing into 4 µm-thick sections and mounted onto MS-coated glass slides. Thereafter, the sections were deparaffinized and subjected to H&E staining, according to standard procedures. Images were captured under a light microscope (BX-52; Olympus, Tokyo, Japan).

Immunohistochemical (IHC) staining of FMT organoids

IHC staining of organoids was performed as described previously[24,25]. After deparaffinization of organoid sections with xylene and ethanol, the antigen was retrieved in 10 mM citrate buffer with heating at 121 ℃ for 5 min, followed by inactivation of the endogenous peroxidase activity by treating the sections with 1% peroxidase for 30 min. Subsequently, after blocking with 10% normal goat serum (NGS) for 30 min at room temperature, the samples were incubated at 4 ℃ overnight with HER2 (1:200). The sections were then washed three times with PBS, incubated with secondary antibody (EnVision Dual Link System-HRP), and visualized using DAB solution (Nacalai Tesque, Tokyo, Japan). Nuclei were counterstained with Mayer's hematoxylin. All images were captured using a light microscope (BX-43; Olympus).

Live/dead staining

After perfusion of organoids with anti-cancer drugs, they were transferred from the device to 48-well plates, and 100 µL of LIVE/DEAD™ Cell Imaging Kit (488/570) reagents (Thermo Fisher Scientific) were added per well and incubated for 15 min at room temperature. After incubation, cells were observed under a fluorescence microscope (BZ-9000; Keyence, Osaka, Japan). The cell death rate was calculated by comparing the number of dead cells to the total number of cells.

Quantitative RT-PCR

Total RNA was extracted from the FMT and MI organoids using a NucleoSpin kit (Takara Bio Inc.) following the manufacturer's instructions. First-strand cDNA was synthesized using a QuantiTect Reverse Transcription Kit (QIAGEN). Quantitative real-time PCR was performed using the QuantiTect SYBR I Kit (QIAGEN) and StepOnePlus Real-Time PCR System (Applied Biosystems). The specific primers used for feline *Bax*, *p53*, *Caspase-9*, and *Caspase-8* as well as mouse *Bax*, *p53*, *Caspase-9*, *Caspase-8*, *RIPK3*, *Mlkl*, *Ulk1*, *Atg12,* and *Pick3c3* are listed in Table 1.

Gene	Primer	Sequence
f GAPDH	Forward	5′-CTCATGACCACAGTCCATGC-3′
	Reverse	5′-TGAGCTTCCCATTCAGCTCT-3′
f Bax	Forward	5′-TTTGCTTCAGGGTTTCATCC-3′
	Reverse	5′-GTCCAGTTCATCTCCGATGC-3′
f p53	Forward	5′-AACTGACACCCTCACCCTTG-3′
	Reverse	5′-CTCCCTCACGGTTCCTCATA-3′
f Bcl2	Forward	5′-TTCAGCCGTGTAACTTGCAG-3′
	Reverse	5′-GGAGTGGGAGGAGGAGGTAA-3′
f Caspase-9	Forward	5′-CTAGTTTGCCCACACCCAGT-3′
	Reverse	5′-ACTGCTCGAAAACACCATCC-3′
f Caspase-8	Forward	5′-AGGATGTGCCCAAACTTCAG-3′
	Reverse	5′-TCCATGGGAGAGGATACAGC-3′
f Cyclin D1	Forward	5′-CACACGGACTACAGGGGAGT-3′
	Reverse	5′-TCGCAGCATAAGAGTTGGTG-3′
f Cyclin E1	Forward	5′-TGCTGAAGATGCACACAACA-3′
	Reverse	5′-CTGGTGTGGTCACACTGTCC-3′
m GAPDH	Forward	5′-GAGAGGCCCTATCCCAACTC-3′
	Reverse	5′-GTGGGTGCAGCGAACTTTAT-3′
m Bax	Forward	5′-CACCCCTTTCCTCCTCTCTC-3′
	Reverse	5′-GGAGACACTCGCTCAGCTTC-3′
m p53	Forward	5′-TGGAAGACTCCAGTGGGAAC-3′
	Reverse	5′-TCTTCTGTACGGCGGTCTCT-3′
m Caspase-9	Forward	5′-TGCCCTTGCCTCTGAGTAGT-3′
	Reverse	5′-AACAAAGAAACGCCCACAAC-3′
m Caspase-8	Forward	5′-GGCCTCCATCTATGACCTGA-3′
	Reverse	5′-TGTGGTTCTGTTGCTCGAAG-3′
m RIPK3	Forward	5′-GGGACCTCAAGCCCTCTAAC-3′
	Reverse	5′-GATCCTGATCCTGACCCTGA-3′
m Mlkl	Forward	5′-GTTTGTGAGTGTGGGCAATG-3′
	Reverse	5′-GCATTGCTTCAGGGTTTTGT-3′
m Ulk1	Forward	5′-TGCTGGCAGGTAGACATCAG-3′
	Reverse	5′-GAAAAGCTTGCTTTGGCTTG-3′
m Atg12	Forward	5′-TAGAGCCCTACCCAGTGTGG-3′
	Reverse	5′-TGAATGCTGGAGAGATGCAG-3′
m Pik3c3	Forward	5′-TCCTTGATGGTTGATGCAAA-3′
	Reverse	5′-AGTGCACAGCCTCCTCATCT-3′

Table 1. Primers for real-time quantitative PCR analysis.

Numerical analysis using COMSOL

A COMSOL simulation was conducted to present the transport and diffusion of anti-cancer drugs, providing insights into the time-dependent concentration gradients within gels and organoids. The geometry used in the simulation corresponds to the actual dimensions of the microfluidic device (Supplemental Fig. 1a). The simulation involved a liquid with the same density and viscosity as water, carrying the drugs entering through an inlet, flowing through four chambers (PAs and PB), and exiting through three outlets. Each chamber contains a hemispherical cap (1.5 mm radius, 1 mm height), embedded with 50 solid microspheres (40–45 µm radius), representing the structural components of gels and organoids, and simulating species diffusion within them (Supplemental Fig. 1b). Detailed quantitative comparison supported by precise mathematical modeling and simulation-based results shows that COMSOL simulation results revealed good alignment with experimental data (Supplemental Fig. 1c). The model utilizes Laminar Flow and Transport of Diluted Species interfaces to fully capture the fluid flow and diffusion. The simulations involve solving the fluid flow within the microfluidic device, with an inlet flow rate of approximately 570 µL/min. This results in a low Reynolds number, indicating a laminar flow. The fluid motion is modeled by solving the incompressible Navier–Stokes equations, which govern the behavior of viscous flows under the assumptions of steady state and incompressibility:

$$\frac{\partial}{\partial t}\left(\rho\vec{U}\right) + \nabla \cdot \left(\rho\vec{U}\vec{U}\right) = -\nabla P + \nabla \cdot \left[\mu\left(\nabla\vec{U} + \nabla\vec{U}^{T}\right)\right]$$

$$\nabla \cdot \vec{U} = 0$$

Here ρ denotes density, u is the velocity, μ denotes viscosity, and p equals pressure.

The drugs are present at relatively low concentrations (10 μM) compared to the solvent, and changes in concentration do not significantly affect the fluid's density or viscosity. This makes it appropriate to apply Fick's law to describe the diffusive transport as follows:

$$-\nabla \cdot (-D\nabla c + c\overrightarrow{U}) = 0$$

where D denotes the diffusion coefficient and c represents the concentration. The diffusion coefficient of the species D_c can be estimated based on the Stokes–Einstein relationship[43]:

$$D_c = \frac{kT}{6\pi\mu R}$$

where k is the Boltzmann constant, T is the Kelvin temperature, R is the Stokes radius, and μ is the dynamic viscosity of media. The diffusion coefficient for the gel D_g was adjusted by multiplying the media coefficient by a diffusion hindrance factor derived from the area fraction based on the gel fiber diameter in isotropic networks[44]. A significantly lower diffusion coefficient D_o was applied to the organoids to facilitate the establishment of a concentration threshold representing the rate of cell death.

Numerical analysis of liquid flow and drug diffusion

Because the rate of cell death by perfusion of anti-cancer drugs drastically differed before and after branching in the device, we hypothesized that differences in flow velocity and drug infiltration would affect the survival rates of FMT organoids. To explore the influence of flow velocity and drug diffusion on FMT-organoid survival, we conducted a numerical analysis using COMSOL Multiphysics.

Supplemental Fig. 2a shows the velocity distribution within the microfluidic device, revealing significant differences in the flow rate before (PB) and after branching (PA). The flow rate at cross-section B-B (entrance to PB) was 559.8 μL/h, while cross-section A1-A1 (entrance to PA1) and A2-A2 (entrance to PA2) had flow rates of 233.5 and 157.6 μL/h, respectively. These variations resulted in differential extents of drug diffusion across the chambers after 48 h (Supplemental Fig. 2b). PB exhibited the highest degree of species penetration, with minimal concentration differences between the periphery and the center of the gel (Supplemental Fig. 2c). Conversely, PA1 and PA2, which had lower flow rates, exhibited reduced drug diffusion into the gel center. The lowest drug penetration was observed in non-perfused chambers.

To further assess the correlation between drug concentration and organoid mortality, we set concentration thresholds that indicated cellular death when exceeded (Supplemental Fig. 2d). The simulation results were consistent with the experimental findings, where higher drug penetration in PB corresponded to increased cell death, whereas PA regions exhibited reduced mortality owing to lower flow rates.

Statistical analysis

Data are presented as mean ± SD. Statistical evaluation was conducted using SigmaPlot software with one-way analysis of variance (ANOVA) followed by a t-test or Mann–Whitney test. When P values were < 0.05, it was considered statistically significant.

Results

Establishment of a microfluidic system using FMT organoids

To establish a microfluidic system using organoids, FMT organoids generated from mammary tumor-affected cats were mounted on device wells and perfused with a culture medium containing anti-cancer drugs for 48 h. The effects of drug perfusion on FMT organoids were examined by measuring cell viability and genetic analysis (Fig. 1A). After generating FMT organoids, we confirmed their characteristics. H&E staining of FMT organoids showed that the mammary tumor cells grew in a three-dimensional fashion and formed aggregates (Fig. 1B-Left panel). Immunohistochemical staining revealed the expression of the mammary tumor marker HER2 in FMT organoids (Fig. 1B-Right panel). These results indicated that FMT organoids can recapitulate the characteristics of mammary tumors in cats. The microfluidic devices used in this study were created using CAD design and acrylic cutting. As shown in Fig. 1C, we designed suitable and interconnected chamber sizes and depths to allow for multiple organoid cultures. The device presented a branched structure; the liquid entering the device from the inlet port branched into three different channels and was discharged from the three outlets (Fig. 1D). After mounting organoids on the device and filling with culture media by syringe, they were perfused for 48 h in a CO_2 incubator at 37 °C (Fig. 1E).

Effects of perfusion on cell viability of FMT organoids

We first examined the effects of perfusion on the viability of FMT organoids. After loading the FMT organoids, the organoid culture medium (without anti-cancer drugs) was perfused at 9.5 μL/min for 48 h. After perfusion, cell viability and expression of apoptosis-related genes were compared in three groups: organoids under non-perfusion conditions (NP), organoids perfused in the chamber before branching (PB), and organoids perfused in the chamber after branching (PA) (Fig. 2A). Live/dead staining of FMT organoids after perfusion revealed that perfusion of the culture medium had little effect on FMT organoid viability (Fig. 2B). Interestingly, the highest cell death rate was observed under the NP conditions. There were no differences in the rate of cell death between the PB and PA conditions. The expression levels of the apoptosis-related markers *Bax*, *p53*, and *Bcl2*

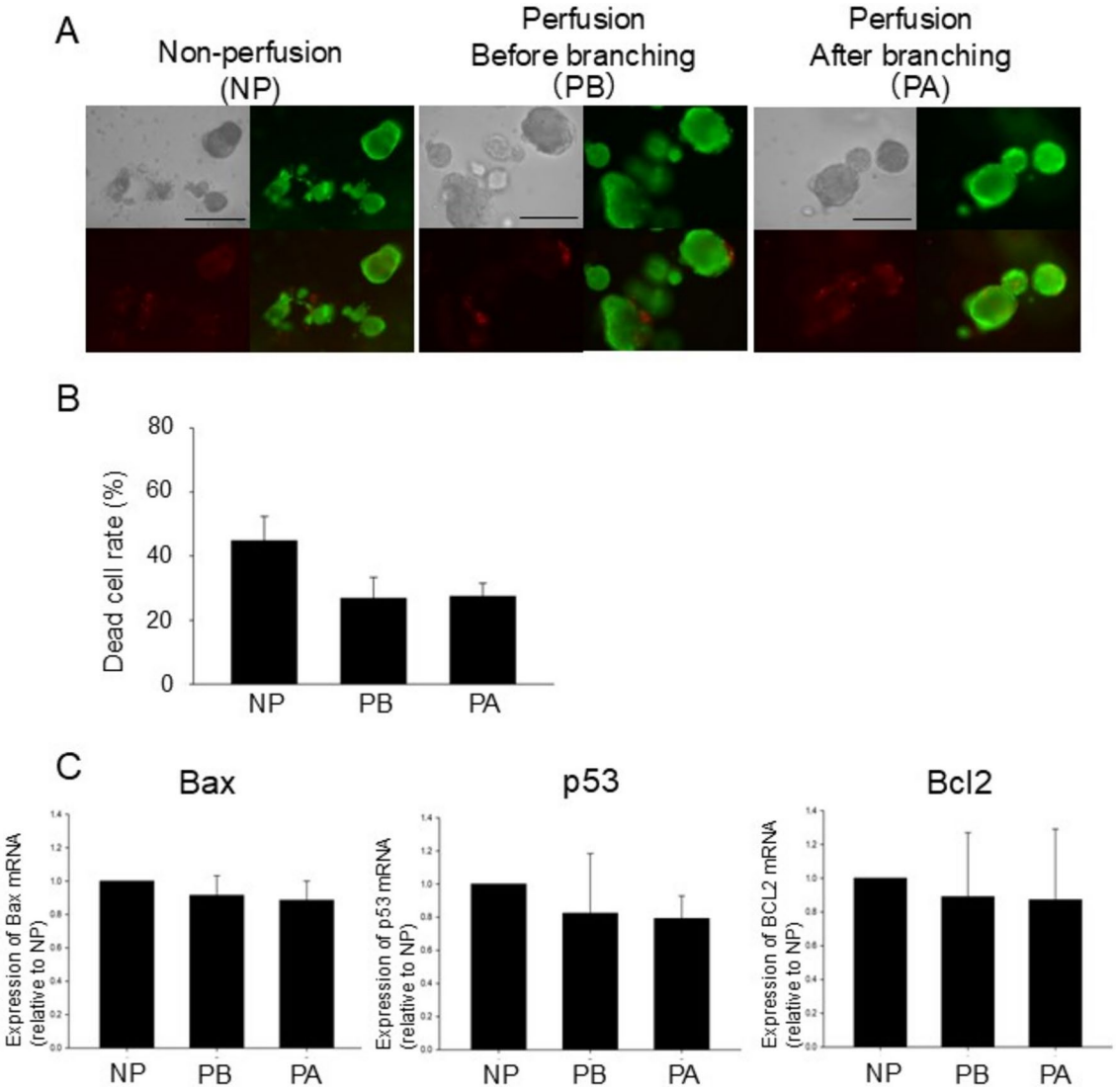

Fig. 2. Effects of culture medium perfusion on cell viability of FMT organoids. Live/dead staining of FMT organoids after culture medium perfusion at 9.5 μL/min for 48 h. From left to right: Non-perfusion (NP), perfusion before branching (PB), and perfusion after branching (PA) (**A**). Green color shows live cells, while red color shows dead cells. Scale bar: 100 μm. Quantification of the cell death rate of FMT organoids after perfusion (**B**). The cell death rate was determined from the ratio of the brightness of live cells to that of dead cells in live/dead staining (n = 6). Results were expressed as mean ± SEM. Effects of perfusion on the expression of apoptosis-related genes in FMT organoids (**C**). The expression levels of *Bax, p53,* and *Bcl2* in each condition of FMT organoids were analyzed by quantitative real-time PCR (n = 6) and quantified based on the ratio of the expression level to *GAPDH*. Data were expressed as mean ± SEM.

were not significantly changed under the three perfusion conditions (Fig. 2C). These results suggest that there was little improvement in the viability of FMT organoids after perfusion with the culture medium.

Effects of perfusion on sensitivity to anti-cancer drugs in FMT organoids

To investigate the effects of perfusion of the culture medium with anti-cancer drugs on the cell viability of FMT organoids, the cells were perfused with doxorubicin or toceranib at 9.5 μL/min. After 48 h of perfusion with toceranib (10 μM) or doxorubicin (1 μM), cell viability was confirmed by live/dead staining (Fig. 3A). In the PB, the dead cell rate was significantly higher than that in the NP for both toceranib and doxorubicin perfusion (Fig. 3A, B). PA tended to increase the rate of cell death, but its effect was lower than that of PB. In FMT organoids of PB with toceranib or doxorubicin, the expressions of *Bax*, *p53*, *Caspase-9*, and *Caspase-8* were significantly elevated compared to those in NP organoids (Fig. 3C, D). However, the expression of these genes in PA organoids was almost the same as that in NP organoids. These results suggest that perfusion of FMT organoids with anti-cancer drugs may promote cell death in FMT organoids, which is mainly caused by apoptosis.

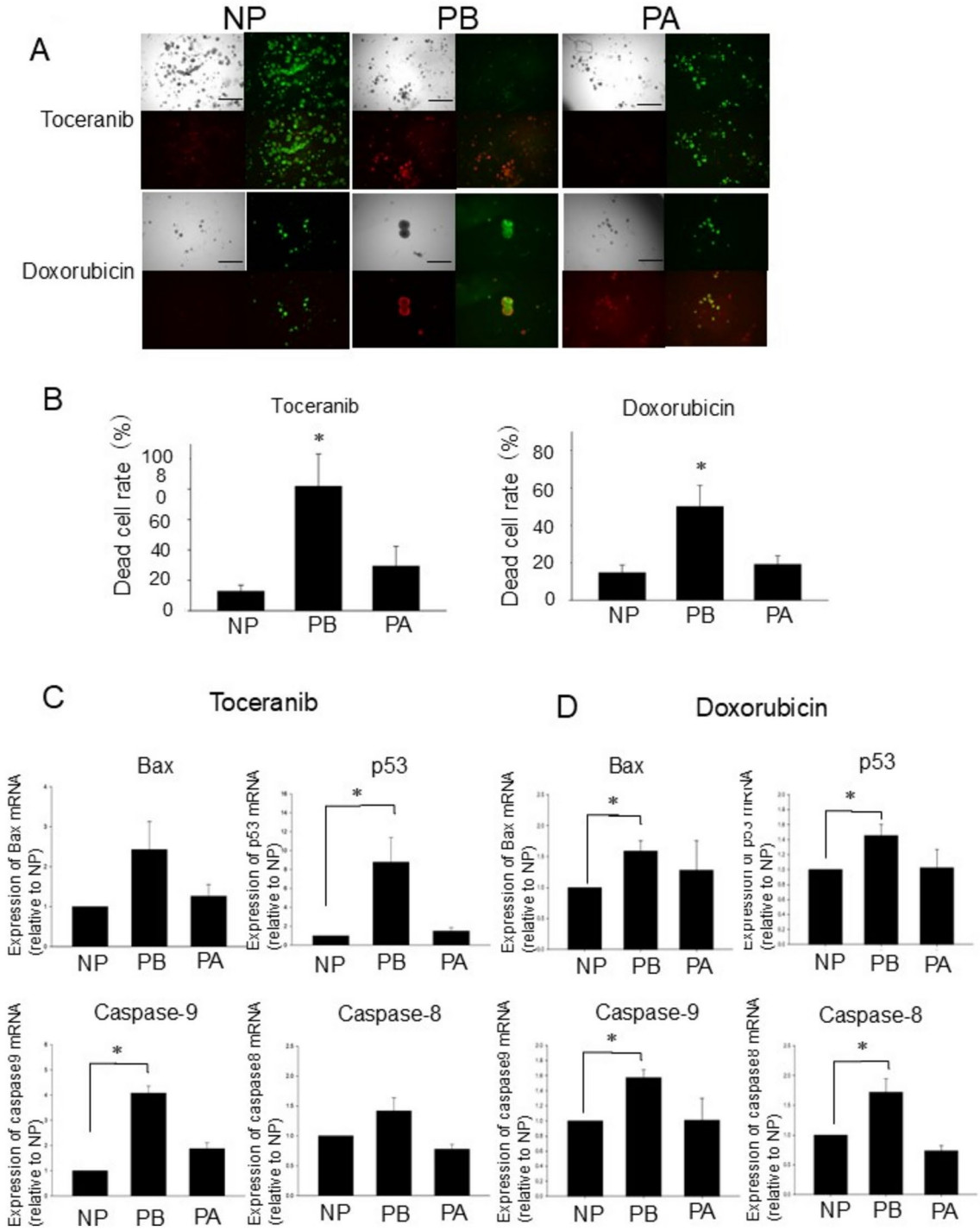

Fig. 3. Effects of culture medium perfusion on the sensitivity of FMT organoids to anti-cancer drugs. Drug sensitivity was examined by perfusion of anti-cancer drugs at 9.5 μL/min for 48 h. Live/dead staining images of FMT organoids after perfusion with the drug were shown. The top row of images is for toceranib (10 μM), whereas the bottom row is for doxorubicin (1 μM) (**A**). Quantification of cell death rate after perfusion of toceranib and doxorubicin (**B**). The cell death rate was determined from the ratio of the brightness of live cells to that of dead cells in live/dead staining. Data were expressed as mean ± SEM (n = 6, $^*P < 0.05$ vs. NP). The effects of drug perfusion on expression levels of apoptosis-related genes. Expression levels of *Bax*, *p53*, *Caspase-9,* and *Caspase-8* in FMT organoids after toceranib (**C**), (n = 6) or doxorubicin (**D**), (n = 6) perfusion were analyzed by quantitative real-time PCR and quantified based on the ratio of the expression level to *GAPDH*. Data were expressed as mean ± SEM ($^*P < 0.05$ vs. NP).

Simulation of drug infiltration and fluid velocity by hydrodynamic simulation (COMSOL)

Because the rate of cell death by perfusion of anti-cancer drugs drastically differed before and after branching in the device, we hypothesized that differences in flow velocity and drug infiltration would affect the survival rates of FMT organoids. To verify this, we visualized flow velocity and drug infiltration in the device using COMSOL fluid dynamics simulation. The simulation showed a decrease in the flow velocity after branching (Fig. 4A). The

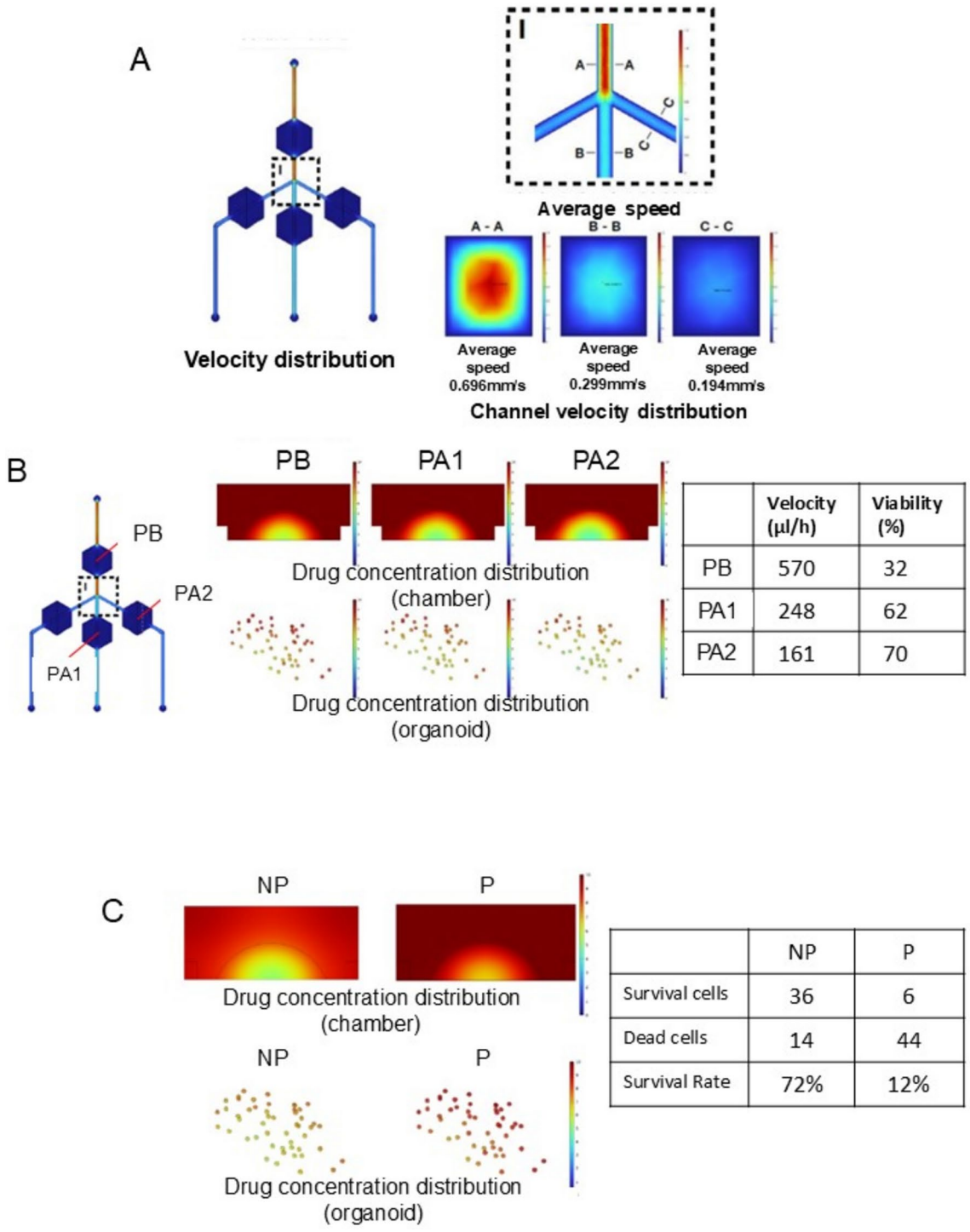

	Velocity (μl/h)	Viability (%)
PB	570	32
PA1	248	62
PA2	161	70

	NP	P
Survival cells	36	6
Dead cells	14	44
Survival Rate	72%	12%

Fig. 4. Drug distribution and fluid velocity simulated by hydrodynamic simulation COMSOL. Perfusion velocities in each position on the device are shown (**A**). Drug concentration and flow velocity in each chamber are also shown (**B**). The organoids are modeled as 90 μm particles, and a fixed number of organoids are randomly placed in the gel. Mortality was defined based on the drug concentration that permeated the organoid mimetic particles. Comparison of chambers with and without perfusion (**C**). Perfusion allows the drug to penetrate the gel, and the drug concentration in the organoids is higher.

simulated flow velocity before branching (A-A) was 0.696 mm/s, whereas, the flow velocities after branching were 0.299 mm/s (B-B) and 0.194 mm/s (C-C) (Fig. 4A). Simulations of flow velocity and organoid viability in PB and PA showed that the flow velocity was higher in PB than in PA, resulting in more drug infiltration into the gel and organoids, and thus lower organoid viability (Fig. 4B). In addition, simulations of the drug concentration in the non-perfusion device (NP) and perfused device (P) showed that the drug concentrations in the chamber, gel, and organoids were also higher owing to perfusion (Fig. 4C). These simulation results were consistent with the increased cell death rates of FMT organoids due to perfusion of anti-cancer drugs and the decreased survival of PB organoids compared to that of PA organoids in the same device.

Assessment of side effects of anti-cancer drug using the organoid-on-a-chip system

As side effects accompany anti-cancer drug therapy, it is necessary to simulate the side effects in the body when anti-cancer drugs are administered. Therefore, we attempted to simultaneously evaluate the side effects of anti-cancer drugs on normal tissues as well as the sensitivity of cancerous tissues to anti-cancer drugs on a microfluidic device (Fig. 5A). After loading FMT and MI organoids in each chamber on the same device, toceranib (10 μM) was perfused at the rate of 9.5 μL/min (Fig. 5A). After 48 h of perfusion, the viability of the MI organoids was analyzed using live/dead staining (Fig. 5B). As expected, the cell death rate was significantly higher in MI organoids perfused (P) with toceranib than in non-perfused (NP) ones, indicating that the cell death rate of normal tissue-derived organoids also increased with drug perfusion. Interestingly, toceranib perfusion did not increase the expression levels of apoptosis-related genes in MI organoids (Fig. 5C). However, the expression levels of necrosis-related genes such as *RIPK3* and *Mlkl* were increased upon toceranib perfusion. These data indicate that perfusion with toceranib reduces the viability of MI organoids by inducing necrosis rather than apoptosis (Fig. 5D).

Effects of necrosis inhibition on toceranib perfusion-induced cell death in MI organoids

To confirm that decreased viability in MI organoids caused by toceranib perfusion was related to necrosis, a necrosis inhibitor, HS-1371 (10 nM) was simultaneously perfused with toceranib (10 μM) at 9.5 μL/min for 48 h in the device mounted with FMT and MI organoids. The obtained data revealed that HS-1371 did not affect the cell death rate of FMT organoids, whereas the cell death rate of MI organoids was decreased (Fig. 6A). In addition, simultaneous perfusion with HS-137 and toceranib decreased the expression of *RIPK3* and *Mlkl* genes in MI organoids (Fig. 6B). These results indicate that cell death induced by toceranib perfusion in MI organoids primarily involves necrosis rather than apoptosis.

Discussion

In the present study, we demonstrated that an organ-on-chip system of cancer and normal organoids can be used to simultaneously evaluate the sensitivity to and side effects of anti-cancer drugs. The main findings of the study are as follows: (1) When the culture medium was perfused into FMT organoids, cell viability and expression of genes related to apoptosis were not significantly affected (Fig. 2). (2) When FMT organoids were perfused with anti-cancer drugs toceranib and doxorubicin, apoptosis was induced and cell viability was markedly reduced (Fig. 3). (3) Perfusion of MI organoids with toceranib also reduced cell viability, as in FMT organoids, but this was due to necrosis induction rather than apoptosis (Fig. 5). (4) Simultaneous perfusion of MI organoids with toceranib and HS-1371, a necrosis inhibitor, suppressed cell death and expression of necrosis-related genes compared with toceranib perfusion (Fig. 6). These results suggest that it is possible to evaluate the sensitivity and side effects of anti-cancer drugs in vitro, and that perfusion with anti-cancer drugs promotes apoptosis in cancer cells and induces necrosis in normal intestinal cells (Fig. 6C).

Organ-on-a-chip systems, which mimic blood circulation in the body, more accurately trace the movement of cells exposed to anti-cancer drugs than conventional cell culture models. Therefore, various organ- and disease-derived organ-on-a-chip systems have recently been developed and used for disease modeling and drug discovery[45]. Organ-on-a-chip systems play a role in personalized medicine using patient-derived cells and have the potential to discover new treatments by simplifying and reproducing certain biological mechanisms[46].

The model used in this experiment is a simple design with FMT and MI organoids, and the flow of the culture medium containing the anti-cancer drug mimicked blood circulation in the body. Simultaneous exposure of cancer and normal cells to anti-cancer drugs may be applied in clinical testing. Furthermore, the sensitivity to and side effects of the anti-cancer drug on the individual can be evaluated simultaneously, elucidating the impact of bioactive substances released by cancer cells exposed to the anti-cancer drug on downstream normal cells. The device design may also allow the evaluation of the effects on cancer cells exposed to anti-cancer drugs. Depending on the device design, it may be possible to use cells derived from multiple organs to mimic the in vivo environment better. However, this type of device does not reproduce the feedback from downstream cells to upstream cells that exist in native blood circulation. Therefore, they are inadequate for monitoring more precise cell–cell interactions between different organs and between cancer and normal cells. Complex body-on-chip systems are being developed to reproduce more complex cell–cell interactions in the body by circulating the culture medium to cells derived from multiple organs[47].

Regarding the side effects of anti-cancer drugs on normal cells, not only the effects of the drugs themselves but also their metabolites need to be considered. For example, cyclophosphamide, an alkylating agent, is metabolized in the liver, and its metabolite acrolein is taken up by urothelial cells during renal excretion into the urine, causing drug-induced hemorrhagic cystitis[48–51]. Simplifying the complexity in vivo with an organ-on-a-chip system may help to understand better the effects of bioactive substances and metabolites produced by cancer cells on other cancer and normal cells.

In this study, the perfusion rate was determined based on previous studies. The simulation analysis revealed that the perfusion rate may have changed after device branching (Fig. 4); hence, the survival rate decreased. These

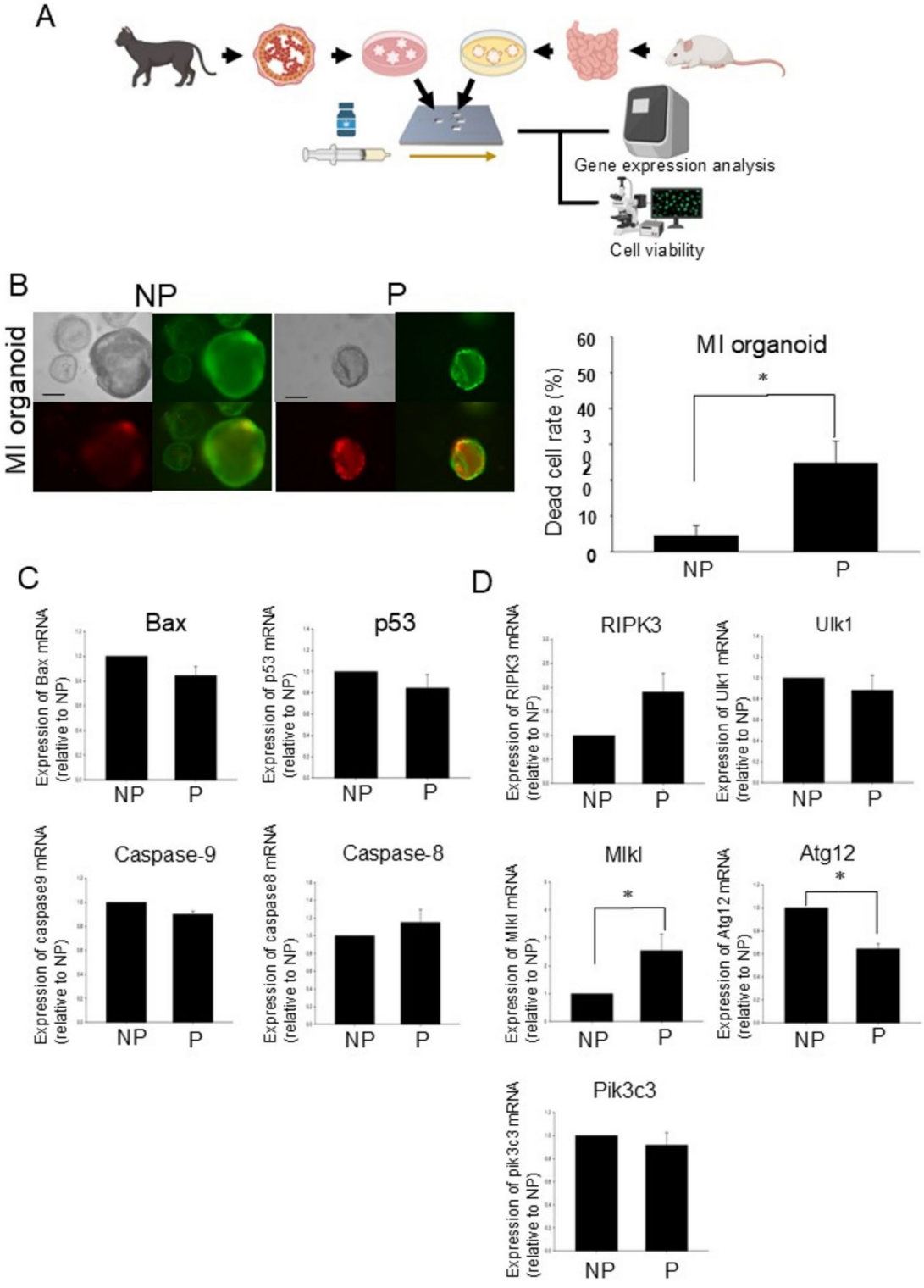

Fig. 5. Assessment of side effects of anti-cancer drug using an organoid-on-a-chip system. Schematic experimental design of perfusion experiments using FMT organoids and normal mouse intestinal (MI) organoids. FMT organoids were mounted in the pre-branching chamber of the device whereas MI organoids were mounted in the post-branching chamber for toceranib perfusion (**A**). Effects of drug perfusion on cell viability of MI organoids. Representative live/dead staining images of MI organoids after perfusion with toceranib for 48 h are shown (**B**). Cell death rate was determined by the ratio of the brightness of viable cells to that of dead cells in live/dead staining. Data were expressed as mean ± SEM (*$P < 0.05$ vs. NP). Expression levels of apoptosis-related genes *Bax*, *p53*, *Caspase-9,* and *Caspase-8* (**C**), (n = 6) and necrosis-related genes *RIPK3*, *Ulk1*, *Mlk1*, *Atg12, and Pik3c3* (**D**), (n = 6) in MI organoids perfused with or without toceranib was analyzed by quantitative real-time PCR and quantified based on the ratio of the expression level to *GAPDH*. Data were expressed as mean ± SEM (*$P < 0.05$ vs. NP).

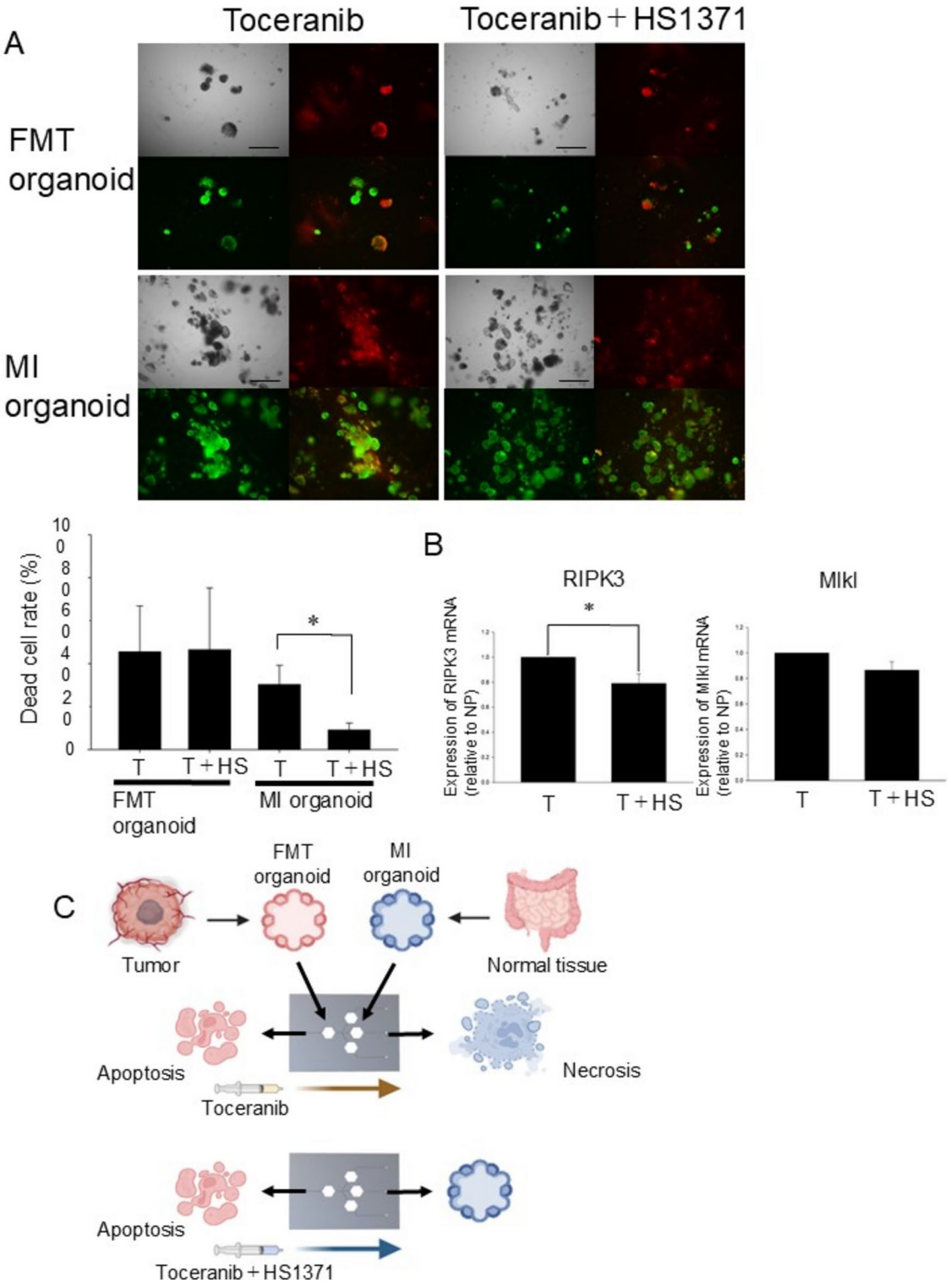

Fig. 6. Effects of the necrosis inhibitor on toceranib perfusion-induced cell death in MI organoids. Live/dead staining of FMT and MI organoids after perfusion with toceranib (10 μM) and a necrosis inhibitor, HS1371 (10 nM) (**A**). Cell death rate was determined from the ratio of the brightness of live cells to that of dead cells in live/dead staining (n = 6). Results were expressed as mean ± SEM. Effects of HS1371 on the expression of necrosis-related genes in MI organoids (**B**). The expression level of *RIPK3* and *Mlkl* in each condition of MI organoids was analyzed by quantitative real-time PCR (n = 6) and quantified based on the ratio of the expression level to *GAPDH*. Data were expressed as mean ± SEM (**P* < 0.05 vs. T). Summary of the present study (**C**).

results suggested that a faster perfusion rate facilitates the penetration of the anti-cancer drugs into organoids and may enhance the efficacy of the drugs. However, the decrease in organoid viability could not be solely attributed to an increased rate of perfusion. When MI organoids were perfused with a culture medium containing no anti-cancer drug, there was no change in cell viability, suggesting that direct stimulation of perfusion alone was not injurious to the organoids themselves. However, real-time PCR results indicated that the expression of necrosis-related genes was increased (data not shown). This suggests that the stress caused by perfusion may cause stress to the organoids in some way. Previous studies have shown that when intestinal cells are cultured under perfusion conditions, a decrease in the perfusion rate promotes intestinal cell differentiation[52]. Based on these results, device design and perfusion rate should be further considered in future experiments.

Toceranib is an animal anti-cancer drug used in dogs and cats and is a class of molecularly targeted drugs based on small-molecule compounds[53]. It is a potent inhibitor of cell surface-expressed tyrosine kinases such as vascular endothelial growth factor receptor 2 (VEGFR-2), fms-like tyrosine kinase receptor 3 (Flt-3), platelet-derived growth factor receptor (PDGFR), stem cell growth factor receptor (c-Kit), neurotrophic factor receptor (RET), colony-stimulating factor receptor (CSF-1R), and others[53]. The fractional inhibition of tyrosine kinases expressed on the cell surface inhibits multiple important signaling pathways involved in the growth and division of tumors and endothelial cells. It has previously shown efficacy primarily in mast cell tumors, anal sac adenocarcinoma, nasal tumors, metastatic lymphomas, and osteosarcoma; however, because it is a multi-targeted inhibitor, it has a broad range of action and is used against a wide variety of tumors[53,54].

Although it is unlikely to cause severe myelosuppression similar to conventional anti-cancer agents, there have been reports of gastrointestinal toxicity, such as diarrhea and vomiting, as well as skin and skeletal muscle damage[55]. In the present study, perfusion of FMT organoids with toceranib reduced cell viability by inducing apoptosis. Furthermore, perfusion of normal intestinal organoids with toceranib induced necrosis, suggesting that these results were due to a cancer-specific molecular target. These results may be due to the cancer-specific properties of the molecularly targeted drugs. Further clarification of the mechanism of action of toceranib in normal tissues may help to reduce its side effects.

When MI organoids were perfused with culture medium only, there was no difference in viability between perfused and non-perfused organoids. However, the expression of *RIPK3* and *Mlkl*, necrosis-related genes, in the perfused organoids increased (data not shown). HS-1371 is an ATP-competitive receptor interaction protein kinase 3 (RIP3) inhibitor and suppresses necrosis by inhibiting RIP3[56]. When HS-1371 was perfused simultaneously with toceranib, there was no change in cell viability in FMT organoids compared with toceranib alone. However, in MI organoids, cell viability was higher when HS-1371 was perfused, indicating that necrosis was suppressed (Fig. 6A, B). Although the pathway of necrosis is not fully understood, it is known that RIPK3 is activated in the early stages of necrosis and forms a complex with RIPK1 and other proteins to activate Mlkl[57].

The expression of apoptosis-related genes such as *p53, Bax*, and *Caspase-8* was similarly elevated. Caspase-8 promotes apoptosis and emerged as a host defense mechanism against RIPK3-RIPK1 kinase complex-dependent necrosis and murine cytomegalovirus[58–61]. However, the interrelationships between these genes remain unknown and require further validation.

In conclusion, we developed a system for anti-cancer drug sensitivity testing using a microfluidic device. This system uses patient-derived organoids and perfuses them with anti-cancer drugs in an environment similar to that of in vivo conditions, thereby enabling a more accurate assay of anti-cancer drug sensitivity and side effects. This study also demonstrated the usefulness of organ-on-a-chip systems in the analysis of cell-to-cell and tissue-to-tissue interactions and provided valuable insights into the influence of mechanical forces on cell viability using an organoid-on-chip model.

Data availability

The authors declare that all the data supporting the findings of this study are available within the article.

Received: 23 October 2024; Accepted: 23 December 2024
Published online: 02 January 2025

References

1. Jemal, A. et al. Cancer statistics, 2003. *CA Cancer J. Clin.* **53**, 5–26. https://doi.org/10.3322/canjclin.53.1.5 (2003).
2. Weijer, K., Head, K. W., Misdorp, W. & Hampe, J. F. Feline malignant mammary tumors. I. Morphology and biology: some comparisons with human and canine mammary carcinomas. *J. Natl. Cancer Inst.* **49**, 1697–1704. https://doi.org/10.1093/jnci/49.6.1697 (1972).
3. Zappulli, V., De Zan, G., Cardazzo, B., Bargelloni, L. & Castagnaro, M. Feline mammary tumours in comparative oncology. *J. Dairy Res.* **72**, 98–106. https://doi.org/10.1017/s0022029905001263 (2005).
4. Goldschmidt, M. H., Peña, L. & Zappulli, V. *Tumors in Domestic Animals* 5th edn, 723–765 (John Wiley Sons Inc, 2016).
5. Mills, S. W. et al. Prognostic value of histologic grading for feline mammary carcinoma: a retrospective survival analysis. *Vet. Pathol.* **52**, 238–249. https://doi.org/10.1177/0300985814543198 (2015).
6. Prop, F. J. et al. Feline mammary carcinomas as a model for human breast cancer. I. Sensitivity of mammary tumor cells in culture to cytostatic drugs. A preliminary investigation of a predictive test. *Anticancer Res.* **6**, 989–994 (1986).
7. De Maria, R. et al. Spontaneous feline mammary carcinoma is a model of HER2 overexpressing poor prognosis human breast cancer. *Cancer Res.* **65**, 907–912. https://doi.org/10.1158/0008-5472.907.65.3 (2005).
8. Zagar, Z. & Schmidt, J. M. A scoping review on tyrosine kinase inhibitors in cats: Current evidence and future directions. *Animals* https://doi.org/10.3390/ani13193059 (2023).
9. Vilhena, H. et al. In *Pets as Sentinels, Forecasters and Promoters of Human Health* (eds Pastorinho, M. R. & Sousa, A. C. A.) 173–207 (Springer International Publishing, 2020).
10. Mulas, J. M. & Reymundo, C. Animal models of human breast carcinoma: canine and feline neoplasms. *Rev. Oncol.* **2**, 274–281. https://doi.org/10.1007/bf02979590 (2000).
11. Hayes, A. A. & Mooney, S. Feline mammary tumors. *Vet. Clin. N. Am. Small Anim. Pract.* **15**, 513–520. https://doi.org/10.1016/s0195-5616(85)50054-6 (1985).

12. Mauldin, G. N., Matus, R. E., Patnaik, A. K., Bond, B. R. & Mooney, S. C. Efficacy and toxicity of doxorubicin and cyclophosphamide used in the treatment of selected malignant tumors in 23 cats. *J. Vet. Intern. Med.* **2**, 60–65. https://doi.org/10.1111/j.1939-1676.1988.tb02794.x (1988).
13. Abugomaa, A. et al. Establishment of a direct 2.5D organoid culture model using companion animal cancer tissues. *Biomed. Pharmacother.* **154**, 113597. https://doi.org/10.1016/j.biopha.2022.113597 (2022).
14. Elbadawy, M. et al. Establishment of Intestinal organoid from *Rousettus leschenaultii* and the susceptibility to bat-associated viruses, SARS-CoV-2 and *Pteropine orthoreovirus*. *Int. J. Mol. Sci.* **22**, 10763. https://doi.org/10.3390/ijms221910763 (2021).
15. Allenspach, K., Zavros, Y., Elbadawy, M., Zdyrski, C. & Mochel, J. P. Leveraging the predictive power of 3D organoids in dogs to develop new treatments for man and man's best friend. *BMC Biol.* **21**, 297. https://doi.org/10.1186/s12915-023-01799-5 (2023).
16. Elbadawy, M., Abugomaa, A., Yamawaki, H., Usui, T. & Sasaki, K. Development of prostate cancer organoid culture models in basic medicine and translational research. *Cancers* **12**, 777. https://doi.org/10.3390/cancers12040777 (2020).
17. Yoshida, T. et al. The potential of organoids in toxicologic pathology: role of toxicologic pathologists in in vitro chemical hepatotoxicity assessment. *J. Toxicol. Pathol.* **35**, 225–235. https://doi.org/10.1293/tox.2022-0017 (2022).
18. Elbadawy, M. et al. Evaluation of the efficacy of mitochondrial fission inhibitor (Mdivi-1) using non-alcoholic steatohepatitis (NASH) liver organoids. *Front. Pharmacol.* **14**, 1243258. https://doi.org/10.3389/fphar.2023.1243258 (2023).
19. Abugomaa, A. et al. Anti-cancer activity of Chaga mushroom (*Inonotus obliquus*) against dog bladder cancer organoids. *Front. Pharmacol.* **14**, 1159516. https://doi.org/10.3389/fphar.2023.1159516 (2023).
20. Abugomaa, A. & Elbadawy, M. Patient-derived organoid analysis of drug resistance in precision medicine: is there a value?. *Expert Rev. Precis. Med. Drug Dev.* **5**, 1–5. https://doi.org/10.1080/23808993.2020.1715794 (2020).
21. Elbadawy, M. et al. Efficacy of primary liver organoid culture from different stages of non-alcoholic steatohepatitis (NASH) mouse model. *Biomaterials* **237**, 119823. https://doi.org/10.1016/j.biomaterials.2020.119823 (2020).
22. Elbadawy, M. et al. Anti-tumor effect of trametinib in bladder cancer organoid and the underlying mechanism. *Cancer Biol. Ther.* **22**, 357–371. https://doi.org/10.1080/15384047.2021.1919004 (2021).
23. Usui, T. et al. Hedgehog signals mediate anti-cancer drug resistance in three-dimensional primary colorectal cancer organoid culture. *Int. J. Mol. Sci.* **19**, 1098. https://doi.org/10.3390/ijms19041098 (2018).
24. Elbadawy, M. et al. Establishment of an experimental model of normal dog bladder organoid using a three-dimensional culture method. *Biomed. Pharmacother.* **151**, 113105. https://doi.org/10.1016/j.biopha.2022.113105 (2022).
25. Elbadawy, M. et al. Establishment of a novel experimental model for muscle-invasive bladder cancer using a dog bladder cancer organoid culture. *Cancer Sci.* **110**, 2806–2821. https://doi.org/10.1111/cas.14118 (2019).
26. Shiota Sato, Y. et al. Derivation of a new model of lung adenocarcinoma using canine lung cancer organoids for translational research in pulmonary medicine. *Biomed. Pharmacother.* **165**, 115079. https://doi.org/10.1016/j.biopha.2023.115079 (2023).
27. Sato, Y. et al. Establishment of an experimental model of canine malignant mesothelioma organoid culture using a three-dimensional culture method. *Biomed. Pharmacother.* **162**, 114651. https://doi.org/10.1016/j.biopha.2023.114651 (2023).
28. Usui, T. et al. Establishment of a dog primary prostate cancer organoid using the urine cancer stem cells. *Cancer Sci.* **108**, 2383–2392. https://doi.org/10.1111/cas.13418 (2017).
29. Leung, C. M. et al. A guide to the organ-on-a-chip. *Nat. Rev. Methods Primers* **2**, 33 (2022).
30. Fang, G. et al. Enabling peristalsis of human colon tumor organoids on microfluidic chips. *Biofabrication* https://doi.org/10.1088/1758-5090/ac2ef9 (2021).
31. Fang, G. C., Chen, Y. C., Lu, H. X. & Jin, D. Y. Advances in spheroids and organoids on a chip. *Adv. Func. Mater.* **33**, 2215043. https://doi.org/10.1002/adfm.202215043 (2023).
32. Park, S. E., Georgescu, A. & Huh, D. Organoids-on-a-chip. *Science* **364**, 960–965. https://doi.org/10.1126/science.aaw7894 (2019).
33. Maulana, T. I. et al. Breast cancer-on-chip for patient-specific efficacy and safety testing of CAR-T cells. *Cell Stem Cell* **31**, 989–1002. https://doi.org/10.1016/j.stem.2024.04.018 (2024).
34. Esch, E. W., Bahinski, A. & Huh, D. Organs-on-chips at the frontiers of drug discovery. *Nat. Rev. Drug Discov.* **14**, 248–260. https://doi.org/10.1038/nrd4539 (2015).
35. Esch, M. B., Mahler, G. J., Stokol, T. & Shuler, M. L. Body-on-a-chip simulation with gastrointestinal tract and liver tissues suggests that ingested nanoparticles have the potential to cause liver injury. *Lab Chip* **14**, 3081–3092. https://doi.org/10.1039/c4lc00371c (2014).
36. Huh, D., Torisawa, Y. S., Hamilton, G. A., Kim, H. J. & Ingber, D. E. Microengineered physiological biomimicry: organs-on-chips. *Lab Chip* **12**, 2156–2164. https://doi.org/10.1039/c2lc40089h (2012).
37. Kimura, H., Sakai, Y. & Fujii, T. Organ/body-on-a-chip based on microfluidic technology for drug discovery. *Drug Metab. Pharmacokinet.* **33**, 43–48. https://doi.org/10.1016/j.dmpk.2017.11.003 (2018).
38. Ronaldson-Bouchard, K. & Vunjak-Novakovic, G. Organs-on-a-chip: A fast track for engineered human tissues in drug development. *Cell Stem Cell* **22**, 310–324. https://doi.org/10.1016/j.stem.2018.02.011 (2018).
39. Skardal, A., Shupe, T. & Atala, A. Organoid-on-a-chip and body-on-a-chip systems for drug screening and disease modeling. *Drug Discov. Today* **21**, 1399–1411. https://doi.org/10.1016/j.drudis.2016.07.003 (2016).
40. Tang, H. et al. Human organs-on-chips for virology. *Trends Microbiol.* **28**, 934–946. https://doi.org/10.1016/j.tim.2020.06.005 (2020).
41. Huh, D., Hamilton, G. A. & Ingber, D. E. From 3D cell culture to organs-on-chips. *Trends Cell Biol.* **21**, 745–754. https://doi.org/10.1016/j.tcb.2011.09.005 (2011).
42. Takebe, T., Zhang, B. & Radisic, M. Synergistic engineering: Organoids meet organs-on-a-chip. *Cell Stem Cell* **21**, 297–300. https://doi.org/10.1016/j.stem.2017.08.016 (2017).
43. Kothapalli, C. R. & Honarmandi, P. Theoretical and experimental quantification of the role of diffusive chemogradients on neuritogenesis within three-dimensional collagen scaffolds. *Acta Biomater.* **10**, 3664–3674. https://doi.org/10.1016/j.actbio.2014.05.009 (2014).
44. Stylianopoulos, T., Diop-Frimpong, B., Munn, L. L. & Jain, R. K. Diffusion anisotropy in collagen gels and tumors: the effect of fiber network orientation. *Biophys. J.* **99**, 3119–3128. https://doi.org/10.1016/j.bpj.2010.08.065 (2010).
45. Mandrycky, C. J., Howard, C. C., Rayner, S. G., Shin, Y. J. & Zheng, Y. Organ-on-a-chip systems for vascular biology. *J. Mol. Cell. Cardiol.* **159**, 1–13. https://doi.org/10.1016/j.yjmcc.2021.06.002 (2021).
46. Zhu, J. et al. Organoids and organs-on-chips: insights into predicting the efficacy of systemic treatment in colorectal cancer. *Cell Death Discov.* **9**, 72. https://doi.org/10.1038/s41420-023-01354-9 (2023).
47. Sung, J. H., Wang, Y. I., Kim, J. H., Lee, J. M. & Shuler, M. L. Application of chemical reaction engineering principles to "body-on-a-chip" systems. *AIChE J.* **64**, 4351–4360. https://doi.org/10.1002/aic.16448 (2018).
48. Zhang, J. et al. Metabolism and transport of oxazaphosphorines and the clinical implications. *Drug Metab. Rev.* **37**, 611–703. https://doi.org/10.1080/03602530500364023 (2005).
49. Boddy, A. V. & Yule, S. M. Metabolism and pharmacokinetics of oxazaphosphorines. *Clin. Pharmacokinet.* **38**, 291–304. https://doi.org/10.2165/00003088-200038040-00001 (2000).
50. Qin, W. S., Deng, Y. H. & Cui, F. C. Sulforaphane protects against acrolein-induced oxidative stress and inflammatory responses: modulation of Nrf-2 and COX-2 expression. *Arch. Med. Sci.* **12**, 871–880. https://doi.org/10.5114/aoms.2016.59919 (2016).
51. Sun, Y. et al. Enhancement of the acrolein-induced production of reactive oxygen species and lung injury by GADD34. *Oxid. Med. Cell. Longev.* **2015**, 170309. https://doi.org/10.1155/2015/170309 (2015).

52. Fois, C. A. M., Schindeler, A., Valtchev, P. & Dehghani, F. Dynamic flow and shear stress as key parameters for intestinal cells morphology and polarization in an organ-on-a-chip model. *Biomed. Microdevices* **23**, 55. https://doi.org/10.1007/s10544-021-00591-y (2021).
53. London, C. et al. Preliminary evidence for biologic activity of toceranib phosphate (Palladia((R))) in solid tumours. *Vet. Comp. Oncol.* **10**, 194–205. https://doi.org/10.1111/j.1476-5829.2011.00275.x (2012).
54. London, C. A. et al. Phase I dose-escalating study of SU11654, a small molecule receptor tyrosine kinase inhibitor, in dogs with spontaneous malignancies. *Clin. Cancer Res.* **9**, 2755–2768 (2003).
55. London, C. A. et al. Multi-center, placebo-controlled, double-blind, randomized study of oral toceranib phosphate (SU11654), a receptor tyrosine kinase inhibitor, for the treatment of dogs with recurrent (either local or distant) mast cell tumor following surgical excision. *Clin. Cancer Res.* **15**, 3856–3865. https://doi.org/10.1158/1078-0432.CCR-08-1860 (2009).
56. Park, H. H. et al. HS-1371, a novel kinase inhibitor of RIP3-mediated necroptosis. *Exp. Mol. Med.* **50**, 1–15. https://doi.org/10.1038/s12276-018-0152-8 (2018).
57. He, S. & Wang, X. RIP kinases as modulators of inflammation and immunity. *Nat. Immunol.* **19**, 912–922. https://doi.org/10.1038/s41590-018-0188-x (2018).
58. Oberst, A. et al. Catalytic activity of the caspase-8-FLIP(L) complex inhibits RIPK3-dependent necrosis. *Nature* **471**, 363–367. https://doi.org/10.1038/nature09852 (2011).
59. Kaiser, W. J. et al. RIP3 mediates the embryonic lethality of caspase-8-deficient mice. *Nature* **471**, 368–372. https://doi.org/10.1038/nature09857 (2011).
60. Chen, I. L., Tsau, J. S., Molkentin, J. D., Komatsu, M. & Hedrick, S. M. Mechanisms of necroptosis in T cells. *J. Exp. Med.* **208**, 633–641. https://doi.org/10.1084/jem.20110251 (2011).
61. Lu, J. V. et al. Complementary roles of Fas-associated death domain (FADD) and receptor interacting protein kinase-3 (RIPK3) in T-cell homeostasis and antiviral immunity. *Proc. Natl. Acad. Sci. U. S. A.* **108**, 15312–15317. https://doi.org/10.1073/pnas.1102779108 (2011).

Author contributions

Yuki Kobayashi, Honoka Hashizume, Haru Yamamoto, Sotaro Takiguchi, Ji Jiajue, Mohamed Elbadawy, and Amira Abugomaa performed the experiments. Ryuji Kawano, Keiichiro Koiwai, Tsutomu Omatsu, Tatsuya Usui, and Kazuaki Sasaki designed the study and analyzed and interpreted the data. Masahiro Kaneda, Mohamed Elbadawy, Tatsuya Usui and Kazuaki Sasaki wrote and revised the manuscript.

Funding

This study was supported by the KAKENHI (grant number JP22K19241).

Declarations

Competing interests

The authors declare no competing interests.

Additional information

Supplementary Information The online version contains supplementary material available at https://doi.org/10.1038/s41598-024-84297-0.

Correspondence and requests for materials should be addressed to M.E. or T.U.